# Assessing the activity of faults in continental interiors: Palaeoseismic insights from SE Kazakhstan

C. Grützner [a,*], E. Carson [b], R.T. Walker [b], E.J. Rhodes [c,d], A. Mukambayev [e], D. Mackenzie [b], J.R. Elliott [b,f], G. Campbell [a], K. Abdrakhmatov [g]

[a] COMET, Bullard Labs, Department of Earth Sciences, University of Cambridge, Madingley Rise, Madingley Road, CB3 0EZ Cambridge, UK
[b] Department of Earth Sciences, University of Oxford, South Parks Road, OX1 3AN Oxford, UK
[c] Department of Geography, University of Sheffield, Sheffield S10 2TN, UK
[d] Earth, Planetary, and Space Sciences, University of California Los Angeles, CA 90095, USA
[e] Kazakhstan National Data Center, Chaikinoy Str. 4, 050020 Almaty, Kazakhstan
[f] COMET, School of Earth & Environment, University of Leeds, LS2 9JT, UK
[g] Kyrgyz Seismological Institute, Academy of Sciences of the Kyrgyz Republic, Asanbay str. 52/1, 720060 Bishkek, Kyrgyzstan

A B S T R A C T

The presence of fault scarps is a first-order criterion for identifying active faults. Yet the preservation of these features depends on the recurrence interval between surface rupturing events, combined with the rates of erosional and depositional processes that act on the landscape. Within arid continental interiors single earthquake scarps can be preserved for thousands of years, and yet the interval between surface ruptures on faults in these regions may be much longer, such that the lack of evidence for surface faulting in the morphology may not preclude activity on those faults. In this study we investigate the 50 km-long 'Toraigyr' thrust fault in the northern Tien Shan. From palaeoseismological trenching we show that two surface rupturing earthquakes occurred in the last $39.9 \pm 2.7$ ka BP, but only the most recent event (3.15–3.6 ka BP) has a clear morphological expression. We conclude that a landscape reset took place in between the two events, likely as a consequence of the climatic change at the end of the last glacial maximum. These findings illustrate that in the Tien Shan evidence for the most recent active faulting can be easily obliterated by climatic processes due to the long earthquake recurrence intervals. Our results illustrate the problems related to the assessment of active tectonic deformation and seismic hazard assessments in continental interior settings.

## 1. Introduction

In this paper we address whether the absence of earthquake surface ruptures and fault scarps can be used to infer the inactivity of faults in tectonically active regions. This issue is not only of interest for understanding the distribution of tectonic deformation, but also for assessing the seismic hazard of a region, which typically relies on the mapping of faults that cut young (Holocene/late Pleistocene) alluvial cover.

The youngest imprints of tectonic activity in the landscape are the remains of surface ruptures from individual earthquakes, which within the interior of Asia can be retained in the landscape for several thousand years (e.g. Campbell et al., 2015; Rizza et al., 2015; Walker et al., 2015). The surface effects of repeated large earthquakes sum to create cumulative fault scarps and/or folding in late Quaternary cover. These characteristic landforms are a primary target of neotectonic studies because they allow identification of the faults, they can be used to determine long-term slip-rates and, when combined with palaeoseismic trenching, allow the timing and magnitudes of past earthquakes to be uncovered (e.g. Wallace, 1977; Thompson et al., 2002).

However, the preservation of surface ruptures and fault scarps from cumulative displacements is governed by the interplay of earthquake magnitude and recurrence interval, erosion of the landscape, and rates of sedimentation. Furthermore, as dramatic climate changes have occurred repeatedly through the Quaternary, the present-day rates of sedimentation and erosion may not be representative of the long-term (Molnar et al., 1994; Poisson and Avouac, 2004). If the recurrence interval between earthquakes is larger than the interval between major periods of environmentally-driven landscape evolution, indications for prior late Quaternary fault activity may be lost (Walker et al., 2015; Abdrakhmatov et al., 2016). The situation is acute in intraplate deformation zones,
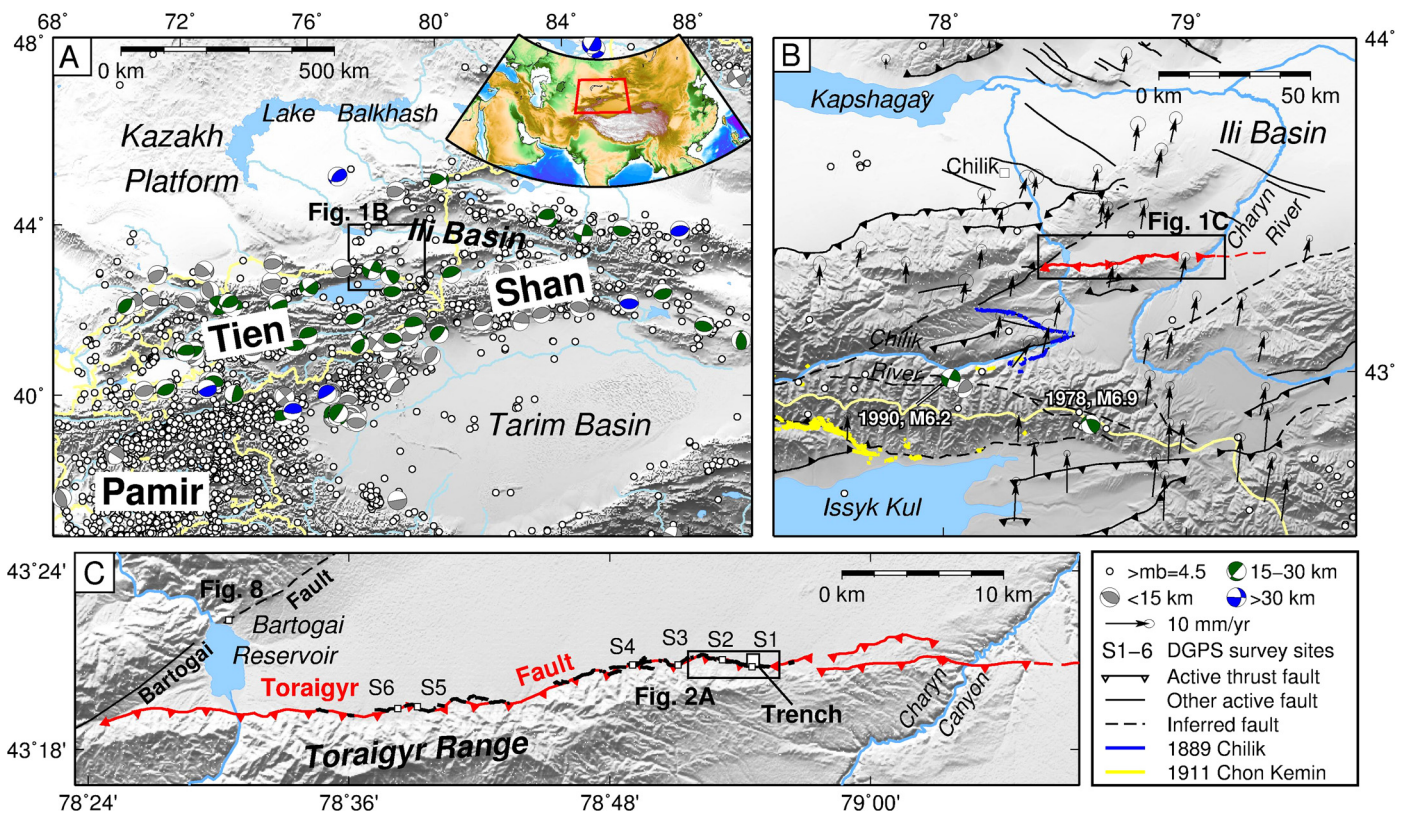
Fig. 1. (A) Topography and earthquakes of the Tien Shan. The study area (black box) is located near the northern margin of the Tien Shan. Focal mechanisms of earthquakes determined from body-waveform modelling are coloured according to centroid depth, data from Sloan et al. (2011). White dots are earthquakes $>M_W$ 4.5 1960–2008 from the catalogue of Engdahl et al. (1998) and the ISC catalogue from 2009–2016 (ISC, 2016). Topography is based on ETOPO1 data. The pale yellow line marks international borders. (B) Active faulting and earthquakes in the study area. The location of the focal mechanism of the 1978 Dzhalanash–Tyup earthquake is from Krüger et al. (2015) and focal data from CMT (2016). All other data sources are as in Fig. 1A. The Toraigyr Fault is marked in red. Inferred ruptures of the 1889 $M_w$ 8.0–8.3 Chilik Earthquake (Bindi et al., 2014; Krüger et al., 2015; Abdrakhmatov et al., 2016) are shown in blue, though the earthquake may also have ruptured faults within the interior of the Kurmenty mountains (Crosby et al., 2007; Abdrakhmatov et al., 2016). Yellow lines mark the surface ruptures of the 1911 Chon Kemin Earthquake (Bogdanovich et al., 1914; Crosby et al., 2007). GPS velocities relative to stable Eurasia with 95% confidence ellipses (Zubovich et al., 2010) show distributed N–S shortening. (C) The S-dipping Toraigyr Fault (red line) is an E–W striking thrust located between the Chilik and Charyn Rivers. The black line marks the mapped scarp. All maps are in Mercator projection. (For interpretation of the references to colour in this figure legend, the reader is referred to the web version of this article.)

where large earthquakes with long recurrence intervals are known to have occurred (e.g. Prentice et al., 2002; Abdrakhmatov et al., 2016).

We address these issues through a study of the Toraigyr Fault, sited within the semi-arid Ili Basin, in the NE Tien Shan of Kazakhstan (Fig. 1). The Toraigyr Fault is expressed in alluvial fans as a well-preserved and continuous scarp. However, as we show later, the scarp results from a single prehistoric surface-rupturing earthquake, with only very localised evidence preserved in the landscape for prior late Quaternary activity. We combine data from satellite remote sensing, low-altitude photogrammetry, field mapping, palaeoseismological trenching, and Quaternary dating techniques to survey the palaeo-ruptures along the Toraigyr Fault, and to bracket the age of this event, and an older event exposed by trenching. We show the consequences of the interplay between tectonic uplift and erosion events on the preservation of earthquake surface ruptures, and the implication of these findings for neotectonic studies and seismic hazard assessments in Central Asia.

## 2. Geological and tectonic setting

Our study area is located in the NE Tien Shan in Kazakhstan. The Tien Shan is bordered by the stable Kazakh Platform to the North and by the relatively rigid Tarim Basin and the rapidly deforming Pamirs to the South (Fig. 1A). The most recent and still ongoing episode of orogeny was initiated in the Neogene as a re-

sult of the India–Eurasia collision, which is happening more than 1000 km to the South today. The Tien Shan is made up of sub-parallel east–west elongated mountain ranges and inter- and intramontane sedimentary basins (Tapponnier and Molnar, 1979). Most of the ranges are fault-bounded and formed of Palaeozoic rocks (Burtman, 1975). The largest basins show Cenozoic successions of up to several kilometres thickness (e.g. Hendrix et al., 1992). An extensive Mesozoic erosional surface is preserved in many locations across the orogeny and can be conveniently used as a marker to estimate cumulative Cenozoic uplift and deformation (e.g. Selander et al., 2012).

GPS data show shortening of about 12 mm/a in the eastern Tien Shan (Abdrakhmatov et al., 1996; Zubovich et al., 2010), which increases to ∼20 mm/yr in the western part due to the rotation of the Tarim Basin. Shortening is accommodated at the surface by a combination of east–west thrust faults, and conjugate left- and right-lateral strike-slip faults (Molnar and Tapponnier, 1975; Tapponnier and Molnar, 1979; Avouac and Tapponnier, 1993; Avouac et al., 1993; Thompson et al., 2002; Cording et al., 2014). Quaternary slip-rates have been measured or inferred for only a limited number of active reverse faults in the Kazakh Tien Shan (e.g. Cording et al., 2014; Selander et al., 2012).

Instrumental seismicity within the Tien Shan has typically been moderate in magnitude (Fig. 1A), and within the Ili Basin itself there have been few significant earthquakes in recent decades (Fig. 1B). To the south of our study area, the Dzhalanash–Tyup earthquake of $M_W$ 6.9 with an oblique-slip mechanism
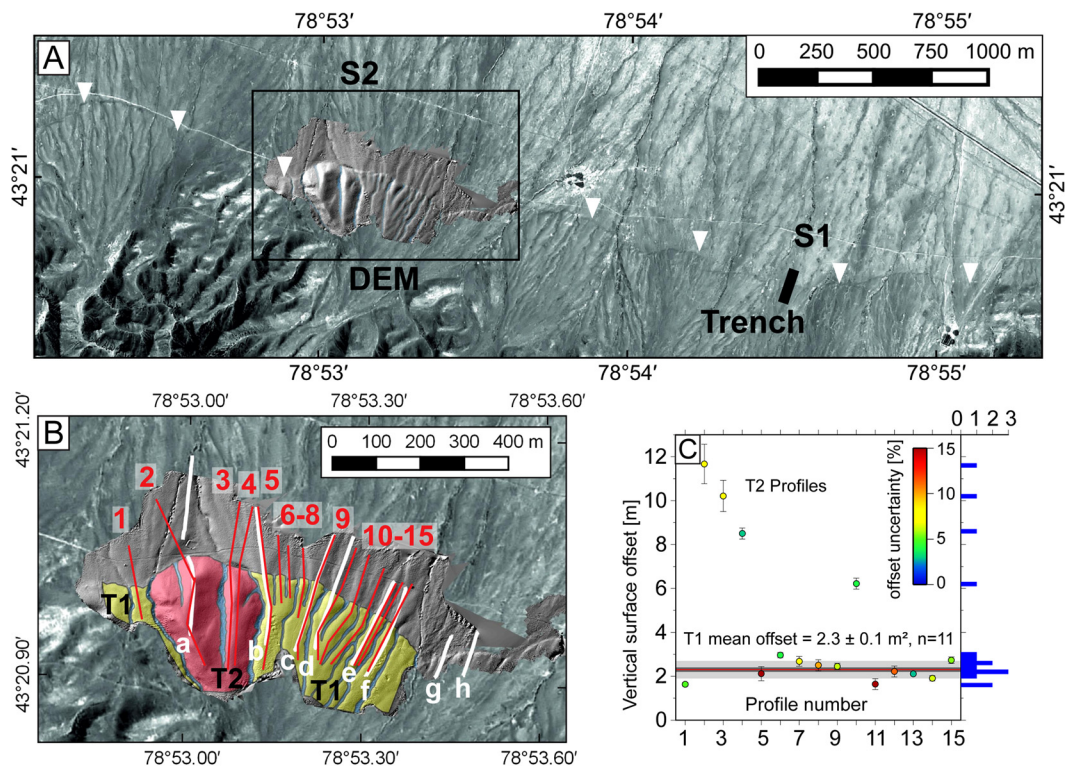
**Fig. 2.** (A) Panchromatic Kompsat-2 satellite image (1 m resolution) showing the active fault scarp (arrows) and overlaid DEM from SfM. Black bar indicates the trench site in offset alluvial fans ($T1$), characterised by a continuous scarp of ~1.5 m height. Inset marks the position of B; the black bar indicates the location, but not the size of the trench. (B) SfM DEM with profiles from DGPS in white and profiles from the DEM in red. Two terrace levels T1 and T2 can be distinguished. See appendix A for profiles. (C) Vertical fault surface offsets measured from the 15 fault-perpendicular profiles (marked by red lines in (b)) taken across the aerial-derived DEM. Individual point offsets are coloured by the percentage uncertainty in the estimation of the vertical fault offset. Red line: mean offset for T1 (from the 11 points <3 m); light grey band: $1\sigma$ standard deviation in offsets, dark grey band standard error in the estimate of the mean (0.1 m). Histograms of vertical surface offsets are shown by the blue bars on the right, bins are in 0.1 m intervals. (For interpretation of the references to colour in this figure legend, the reader is referred to the web version of this article.)

struck the Kyrgyz–Kazakh border area on 24th March 1978 (e.g. Abdrakhmatov et al., 2016). On 12th November 1990 a $M_w$ 6.2 strike-slip earthquake occurred in the Saty area near the Chilik River at a depth of 18 km (Sloan et al., 2011; Fig. 1B). In both cases, no surface ruptures were reported. Instrumentally-recorded earthquake centroid depths within the Tien Shan appear to be restricted to less than 30 km, though deeper events are known from the forelands (e.g. Sloan et al., 2011).

The potential for large earthquakes to occur in the NE Tien Shan is shown from historical events (Fig. 1B). The largest historical earthquake close to our study area is the 11 July 1889 Chilik Earthquake. This event was one of the strongest continental earthquakes ever recorded with a magnitude of $M_w$ 8.0–8.3 (Bindi et al., 2014; Krüger et al., 2015). Abdrakhmatov et al. (2016) mapped ~175 km of surface ruptures in the Chilik River valley and related them to the 1889 earthquake based on palaeoseismological trenching results. The 1911 Chon–Kemin earthquake ($M_w$ 7.8–8.0), also referred to as the Kemin or Kebin earthquake, struck north of Issyk Kul in the Chon–Kemin valley (Bogdanovich et al., 1914; Delvaux et al., 2001; Kulikova and Krüger, 2015; Arrowsmith et al., 2016).

Our study area is sited at the western margin of the Ili Basin, which is a ~400 km long and ~120 km wide E-W elongated basin bordered by the Tien Shan in the South and the Dzhungarian Alatau in the North (Fig. 1A). To the west it opens towards the Kazakh platform. The basin is surrounded by almost linear mountain ranges. Some – though not all – of these ranges show clear fault scarps on satellite imagery and in the field (Fig. 1B). The southern boundary of the Ili Basin strikes mainly E-W, with the exception of an ENE-WSW mountain range between the Chilik and Charyn rivers, which is the morphological expression of the left-lateral Chilik–Chon–Kemin fault zone. This range separates a small basin from the main Ili Basin, which narrows to the west and is bound by the Toraigyr Mountains to the south (Fig. 1C). A fault scarp is visible at the northern base of the Toraigyr range (Fig. 2) as the morphological expression of the Toraigyr thrust fault. This fault scarp, which we show to result from a single surface-rupturing earthquake, is the focus of our study. The fault probably continues further to the East beyond the Toraigyr Range for the alluvial fans east of the Charyn River show subtle hints for relatively recent deformation (red line in Fig. 1B). However, since no significant topography is associated with this section, the role of the fault here is unclear and we do not consider it in our further analysis. The Toraigyr Fault was recognized as active by Ostropiko et al. (1987) and Kober et al. (2013), the latter refer to it as Charyn Canyon Fault. Ostropiko et al. (1987) use the term Bartogai Fault for the ENE-WSW striking section of the Chilik–Chon–Kemin fault that crosses the Bartogai Reservoir.

## 3. Data and results

### 3.1. Scarp mapping and profiling

We initially used panchromatic 1 m Kompsat-2 satellite imagery to remotely map the fault scarp (Fig. 2A), with observations verified during fieldwork. The scarp offsets alluvial fans (Figs. 3, 4), and its height and geometry were measured in the field with kinematic differential GPS (DGPS), along with an ~10 cm resolution digital elevation model for one short stretch, as described below.

The visible scarp extends for 25 km along the fault, though is not continuous within that length. The scarp is only well preserved where it displaces alluvial fan surfaces, and there is a ~5 km gap
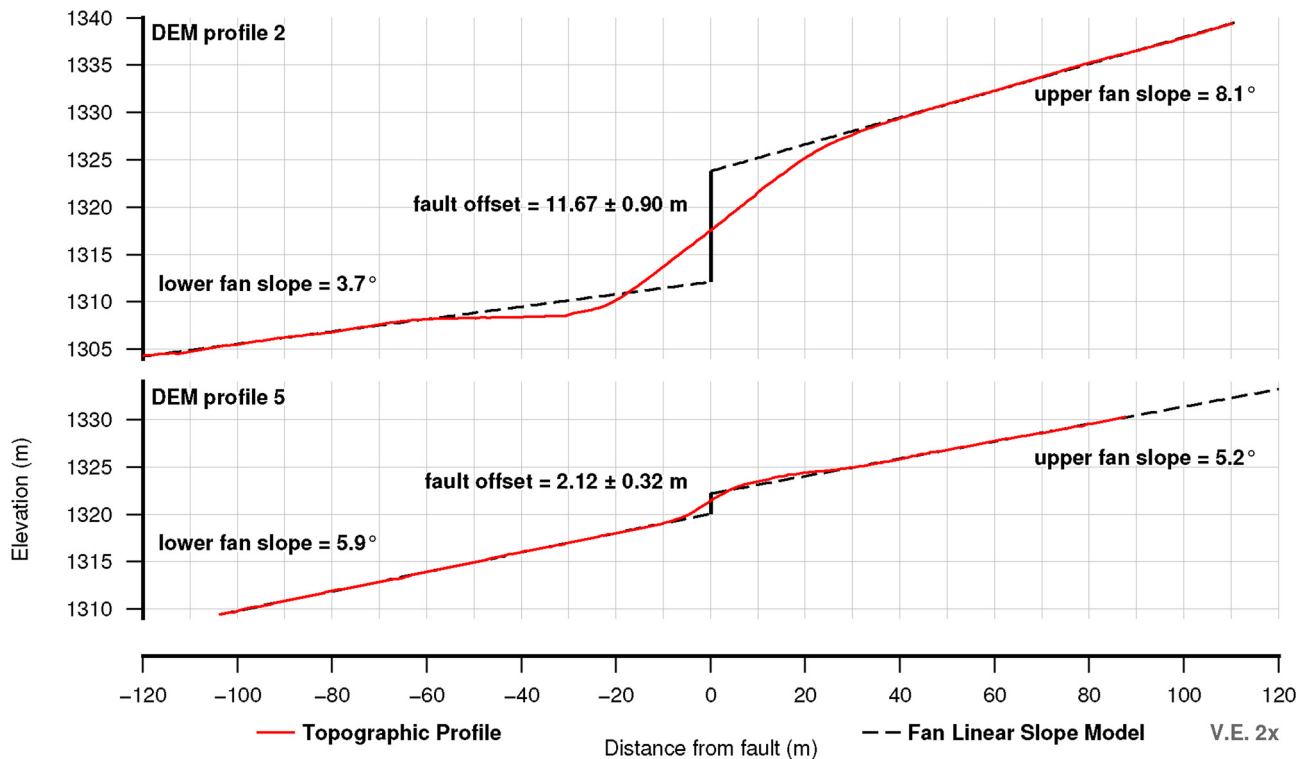
**Fig. 3.** Profiles across the fault extracted from the aerial-derived DEM were used to determine the vertical offset. Profile 2 represents the upper terrace T2, profile 5 is from the lower terrace T1. Angles of slope are given for the upper and lower fan surfaces. See B for location and text for methodology. All DEM profiles are provided in the appendix. (For interpretation of the references to colour in this figure, the reader is referred to the web version of this article.)

in our mapping within the central part of the fault where the scarp rejoins the rangefront (Fig. 1C). Given that the scarp is not well preserved at all points along its length, we infer that the 25 km mapped length is a minimum. We observe curvature that follows the local alluvial fan morphology, which indicates a shallow dip of the fault to the south (Fig. 2A). The scarp faces to the north and consists of continuous segments with lengths of several hundred meters to two kilometres each. No horizontal displacements were encountered.

To survey the ruptures in detail we constructed a digital elevation model (DEM) from low-altitude aerial photography using the 'structure-from-motion' (SfM) technique (e.g. Johnson et al., 2014). A Ricoh GR digital 2 camera was mounted on a kite-stabilised helium balloon (a Helikite), attached to a heavy-duty fishing cable, and walked along a 4 km portion of the fault at an altitude of ∼60 m. The camera took a photo every five seconds. Ground control points (orange 1 × 1 m squares) were laid out and their precise locations measured using DGPS. The photographs were processed using Agisoft PhotoScan to produce a digital elevation model (DEM).

The resulting DEM is shown in Fig. 2B. Fifteen topographic profile lines extracted from the DEM are also indicated (red lines), with two of them shown in Fig. 3. White lines in Fig. 2B mark additional profiles recorded with DGPS. All other topographic profiles are included as supplementary data. Unfortunately we were only able to process the photographs from the western part of the survey due to camera focus malfunction, and so our trench site was not covered. To determine scarp heights we adopted the method of Walker et al. (2015), using a MATLAB script to compute linear regressions of the DGPS points of the upper and lower fan slope, respectively. Where these lines intersect the fault, which is assumed to be located where the scarp gradient is the steepest, we determined the vertical offset. Rather than using the formal uncertainties in determining an offset from the difference in the two linear fits to the upper and lower surfaces, we apply a Monte Carlo

approach to better incorporate the subjective nature in selecting the DGPS points to use in estimating the upper and lower surfaces (as well as better characterising the effect of the slight undulatory nature of some of the fan surfaces, and also the uncertainty in the exact location of the fault). We sample a range of points with differing reasonable bounds of extent on each surface (some shorter, some longer), and do this 10,000 times for each profile, taking the standard deviation in the calculated offsets as a better estimate of uncertainty in the true vertical offset.

The scarp is clearly visible on the hillshaded DEM (Fig. 2B). Two separate alluvial surfaces of different heights are present in the hanging-wall geomorphology. The lower terrace (T1) is extensive and well-preserved. Small ephemeral streams have incised through the fan surface on the southern, uplifted, side of the fault, but away from the stream channels the surface is planar. No prominent knick-points are observed in the stream channels. For T1, the mean scarp height from all the profiles extracted from the aerial-derived DEM is 2.3 ± 0.1 m (Fig. 2C). Three topographic profiles drawn through the small remnant of the T2 surface yield scarp heights of ∼8.5 m, ∼10 m, and ∼12 m (Figs. 2B, C). A single scarp height measurement of ∼6 m (profile 10) may result from a heavily eroded part of T2. It may also belong to a separate terrace intermediate in height between T1 and T2, which is hard to tell in the absence of age constraints. We found no other examples of the 6 m scarp elsewhere along the fault.

The scale and continuity of the scarp in the T1 surface lead us to suggest that it resulted from a single surface-rupturing earthquake, as we confirm from palaeoseismology. Therefore, to provide measurements of scarp height and morphology within the T1 surface along the length of the fault, we made DGPS measurements at six sites S1–S6 (Figs. 1C, 4). At each site, several profiles were measured. Offsets were determined along profiles perpendicular to the scarp for and extending for ∼50–100 m into both the hanging-wall and footwall. The mean scarp height from all the DGPS profiles is 1.6 m, and at most sites the measurements cluster between 1–2 m
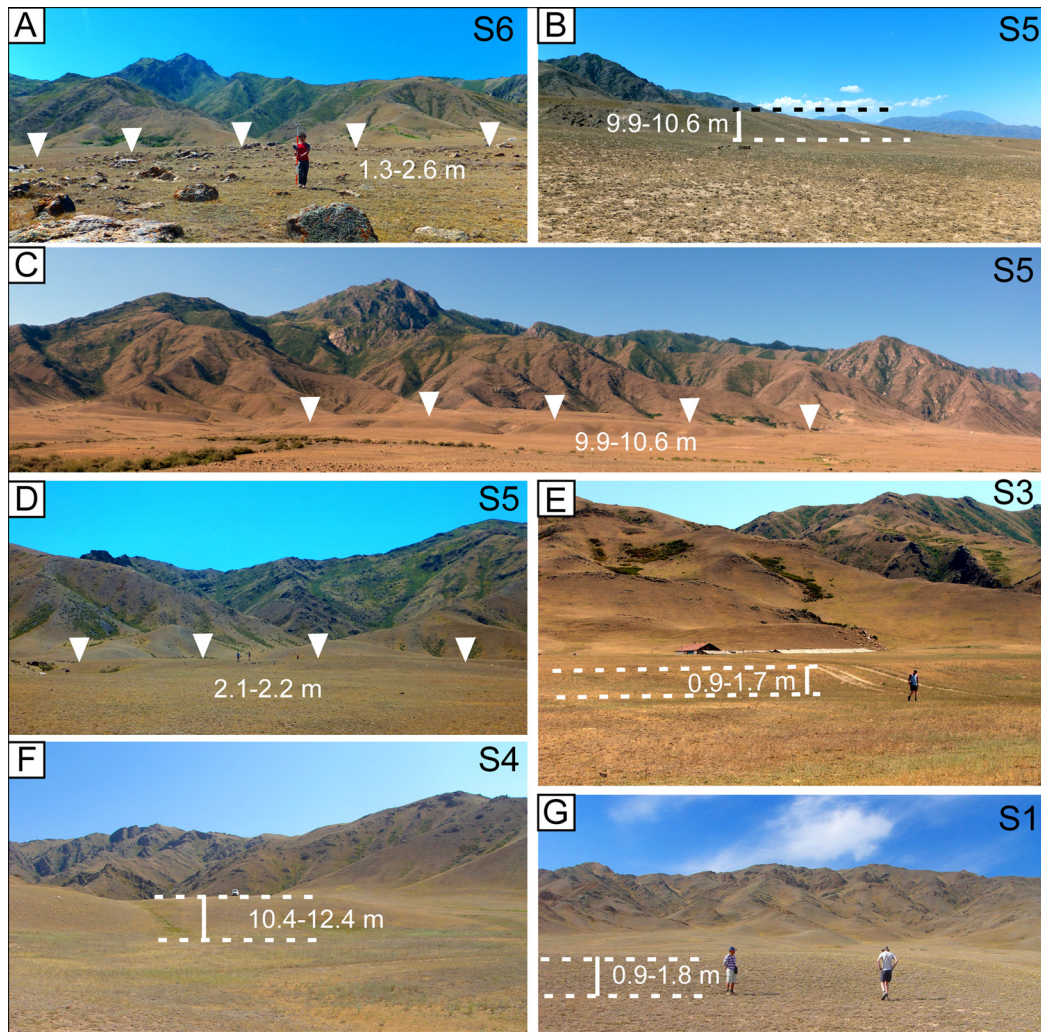
**Fig. 4.** Field photographs and scarp heights estimated from DGPS topographic profiles. See Fig. 1 for individual site locations. All DGPS profiles and vertical offset estimates are provided in the supporting information. S1–S6 refer to the investigation sites marked on Fig. 1C. View is to the south, except for (B), where view is to the east. (G) is the location of the paleoseismological trench.

vertical offset (Fig. 5A). We interpret the consistent scarp heights as evidence for a single-rupture origin.

We found vertical offsets of between 10–14 m at three sites (S2, as shown in the DEM, S3, and S5). None of the T2 remnants are continuous for more than a few hundred meters. We interpret these features as isolated relics of a cumulative scarp, which has been eroded in most places. Without the presence of the smaller, continuous scarp, it would have been hard to identify the isolated fragments as tectonic features.

### 3.2. Palaeoseismic trench

We opened a trench across the fault at N43°20.776′E78°54.543′ in order to confirm that the Toraigyr scarp results from a single earthquake event. From the trench we are also able to estimate the magnitude of the last surface-breaking event, to investigate the deformation associated with the last earthquake, to identify earlier surface-rupturing earthquakes, and to place age constraints on the palaeo-earthquake(s). The trench was excavated close to the main road, along a well-preserved and uniform stretch of the fault scarp in the T1 surface (Fig. 4G). DGPS data from the vicinity of the trench show that the scarp height is around 1.3 m (Figs. 5, 6). Furthermore, the topographic profiles do not show any evidence for folding in the hanging-wall of the fault south of the scarp.

Following excavation the eastern trench wall was cleaned and gridded. A trench log was documented noting lithology, grain size, colour, bedding and deformation. Photographs were taken (also see supplementary data), and using the structure from motion technique (SfM) a 3D model and orthophoto of the trench were produced. In the following we document footwall and hanging wall stratigraphy and describe the observed deformation.

#### 3.2.1. Trench stratigraphy and structure

Two faults were encountered in the trench, both of which offset marker horizons (Fig. 6). Fault zone F1 coincides with the fault scarp and offsets all units but the modern soil. F2 is located south of F1 and only offsets the lowermost units. Fault 1 dips 25° to the south at the base of the trench, and becomes gradually shallower one metre above the trench floor (10° to the south), and then runs approx. horizontal to sub-horizontal (Fig. 6A, B). Fault F2 dips 18° to the south (Fig. 6A, C).

The base of the footwall of F1 is made up of a coarse, poorly sorted alluvial gravel deposit (unit 5). This unit is overlain by a 0.8 m thick silty layer with medium-coarse gravel intercalations. We interpret the homogeneous silty parts as a loess deposit (unit 4). The gravel horizon (unit 4a) probably represents a time of active channel migration – fine silt was deposited on the channel banks and levees, the coarse gravel was deposited where transport energy was high. A reddish palaeosol (unit 3) of ~0.2 m thickness
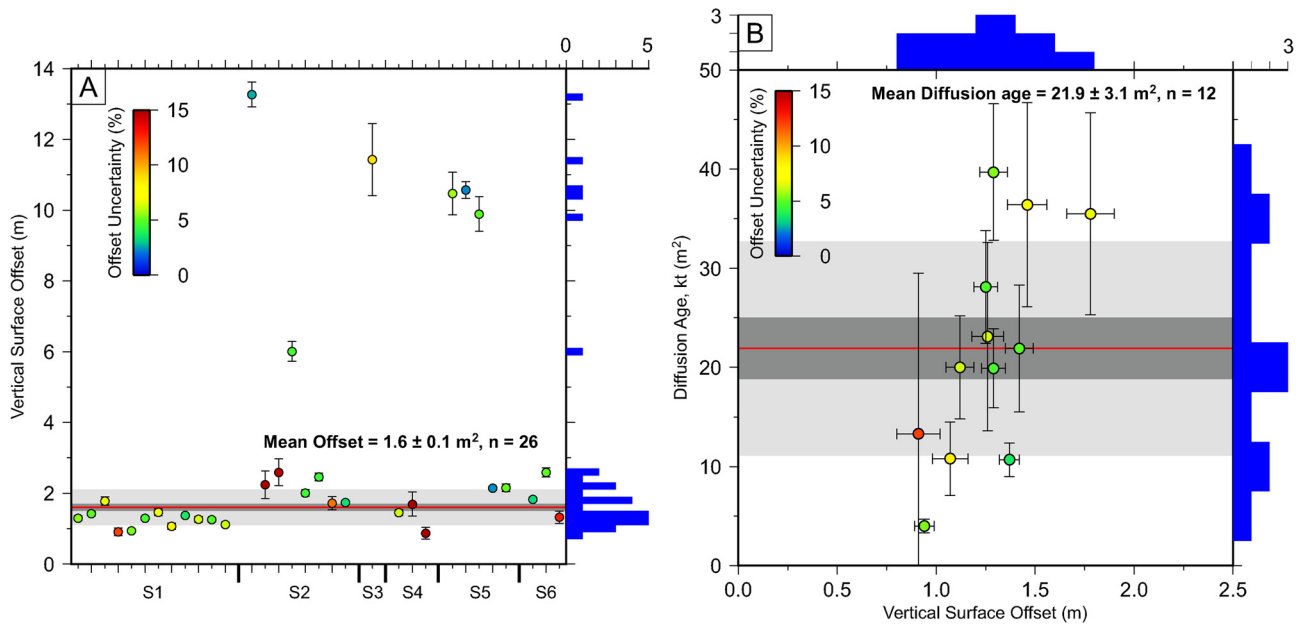
**Fig. 5.** (A) Results for all DGPS profile field sites. The mean offset of T1 is denoted by the horizontal red line with the $1\sigma$ standard deviation shown by the light grey band and the standard error in the mean shown by the dark grey band. Histograms of vertical surface offsets are shown by the blue bars on the right, bins are in 0.2 m intervals. S1–S6 refer to the study sites (see Fig. 1C). (B) Calculated diffusion ages ($\kappa t$) for the twelve DGPS scarp profiles at the trench site with an assumed initial slope angle of 35°. Points are coloured by the percentage error in the estimation of the vertical fault offset. The mean $\kappa t$ value of 21.9 $m^2$ is denoted by the horizontal red line, with the $1\sigma$ standard deviation shown by the light grey band. The 68% confidence on the mean $\kappa t$ value is denoted by the dark grey bar (18–25 $m^2$), the standard error of the mean being 3.1 $m^2$. Histograms of vertical surface offsets and the $\kappa t$ values are shown by the blue bars. (For interpretation of the references to colour in this figure legend, the reader is referred to the web version of this article.)
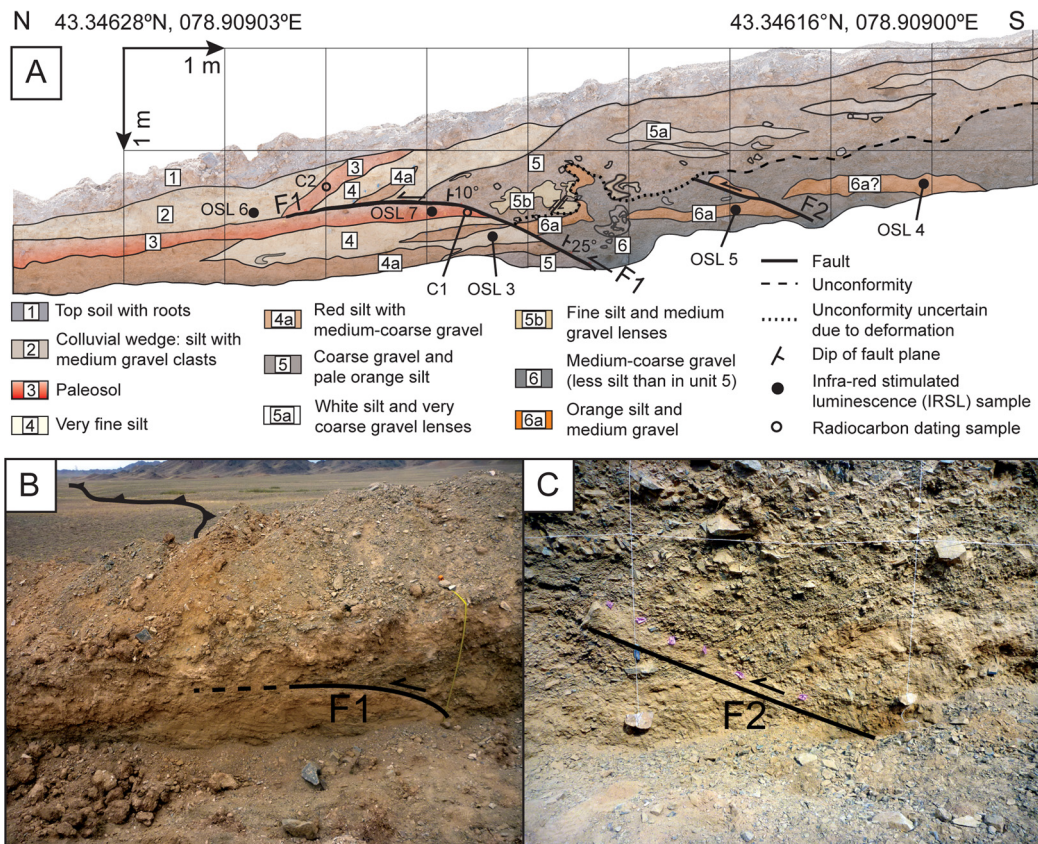


**Fig. 6.** (A) Trench log with the main lithological units, inferred faults, and location of the samples for Quaternary dating. (B) Field photograph showing the fault F1 and its relationship to the morphological scarp. At the trench site, DGPS measurements showed 1.3 m of vertical offset. (C) Field photograph of the fault F2, displacing the lower units in the trench. (For interpretation of the references to colour in this figure, the reader is referred to the web version of this article.)
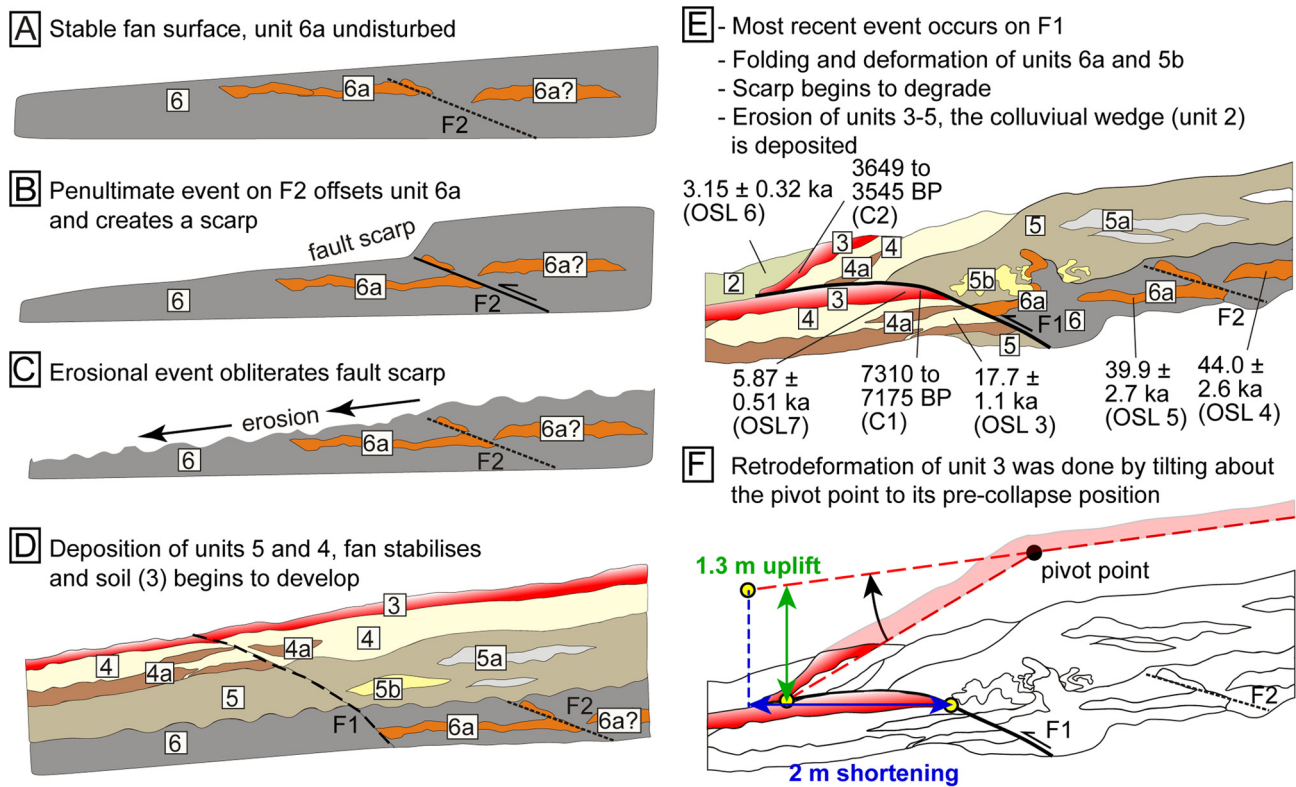
**Fig. 7.** (A)–(E): Retro-deformation of the trench wall with two surface-rupturing events. Radiocarbon ages of stratigraphic units are provided in years before present, IRSL ages are in ka. (F) Sketch illustrating how vertical and horizontal offsets for the last event were determined.

covers the silt-gravel layer. It is offset and truncated at the fault plane and it is the stratigraphically highest layer affected by fault F1. Unit 2 is present only on the footwall and is interpreted as a colluvial wedge that formed after the surface offset by the most recent earthquake. It contains material similar to that found in units 3 and 4 as well as gravels. The unit is less consolidated than units 3 and 4 and has a rather chaotic texture. Therefore, it is likely made up of re-worked material from units 3 and 4 of the hanging-wall. Unit 1 is the recent soil.

The hanging-wall of F1 is covered by the modern soil, unit 1. Units 5–3 are also observed in the hanging-wall. Unit 3 is a pale-osol with the same characteristics as the one in the footwall. Units 4 and 4a in the footwall and in the hanging-wall share their sed-imentological characteristics (grain size, sorting, moisture content, cementation) and are of the same colour. They have a similar thickness and they are bracketed by the same units. Unit 5 is exposed as a whole in the hanging-wall. This poorly sorted alluvial deposit is 0.5–1.0 m thick and contains lenses of whitish silts with very coarse gravels (unit 5a) and intercalations of yellowish fine silt with medium gravels (5b). The latter is strongly affected by warping and even back-thrusting close to the fault F1. Units 3–5 are offset by the fault, tilted and partly warped. This lead to a rather complex stratigraphy in the hanging-wall. Stratigraphically below unit 5 we found a layer of well sorted medium-coarse gravel with significantly less silt and a more grayish colour (unit 6). The contact between units 5 and 6 is an erosional unconformity par-allel to the surface, except close to the fault F1 where small-scale deformation affected both units. Within unit 6 an orange silt layer with medium gravel (unit 6a) stands out, part of which can be used as a marker horizon. This layer is deformed at the fault F1, and offset at the second fault, F2 (Figs. 6–8).

We developed a retro-deformation of the trench log to recon-struct the earthquake history (Fig. 7). The penultimate surface rupturing event occurred at fault F2, offset layers 6 and 6a at

an angle of ∼18° along the fault plane, and produced a scarp (Fig. 7B). Erosion obliterated the scarp after the penultimate earth-quake (Fig. 7C). Restoring the section indicates a vertical offset of ∼0.2 m and a horizontal offset of ∼0.6 m, which equals a total slip of ∼0.63 m. This is a minimum displacement, because the offset wedge of unit 6a could in fact have come from a similar unit stratigraphically below, as is further indicated by IRSL ages determined for the two units 6 and 6a (see later). In this case, the erosional event would have removed most relics of unit 6a in the hanging-wall.

After the erosional event, a period of alluvial fan deposition led to the emplacement of units 5–4 (Fig. 7D), and the formation of a palaeosol (unit 3). The last surface rupturing event occurred on fault F1, offsetting the palaeosol and all units stratigraphically below (Fig. 7E). This event was associated with ∼1.8 m of dis-placement measured along the curved fault plane. With a fault dip of 25° we calculate ∼1.6 m of shortening and 0.8 m of a vertical displacement. However, to measure the total slip we must also ac-count for tilting and internal warping of the layers in the hanging-wall directly beneath the surface scarp, which has resulting in the localised disruption of units 5, 5b, 6 and 6a. In particular 5b has been back-thrusted and warping of units 5b and 6a occurred close to the fault. Furthermore, the pre-event palaeosol (unit 3) is tilted at the scarp. Restoration of the base of the palaeosol to its initial planar geometry by extrapolating its gradient from the hanging-wall to the footwall (Fig. 7F), yields a vertical displacement of ∼1.3 m, in agreement with the DGPS topographic measurements. As this uplift occurred on a 25°S dipping fault, it yields a total fault slip in the shallow subsurface of ∼3 m.

### 3.2.2. Age constraints from the trench

We took two samples from the stratigraphy exposed in the eastern trench wall for radiocarbon dating and seven samples for infra-red stimulated luminescence (IRSL; Table 1, Fig. 6A). Bulk
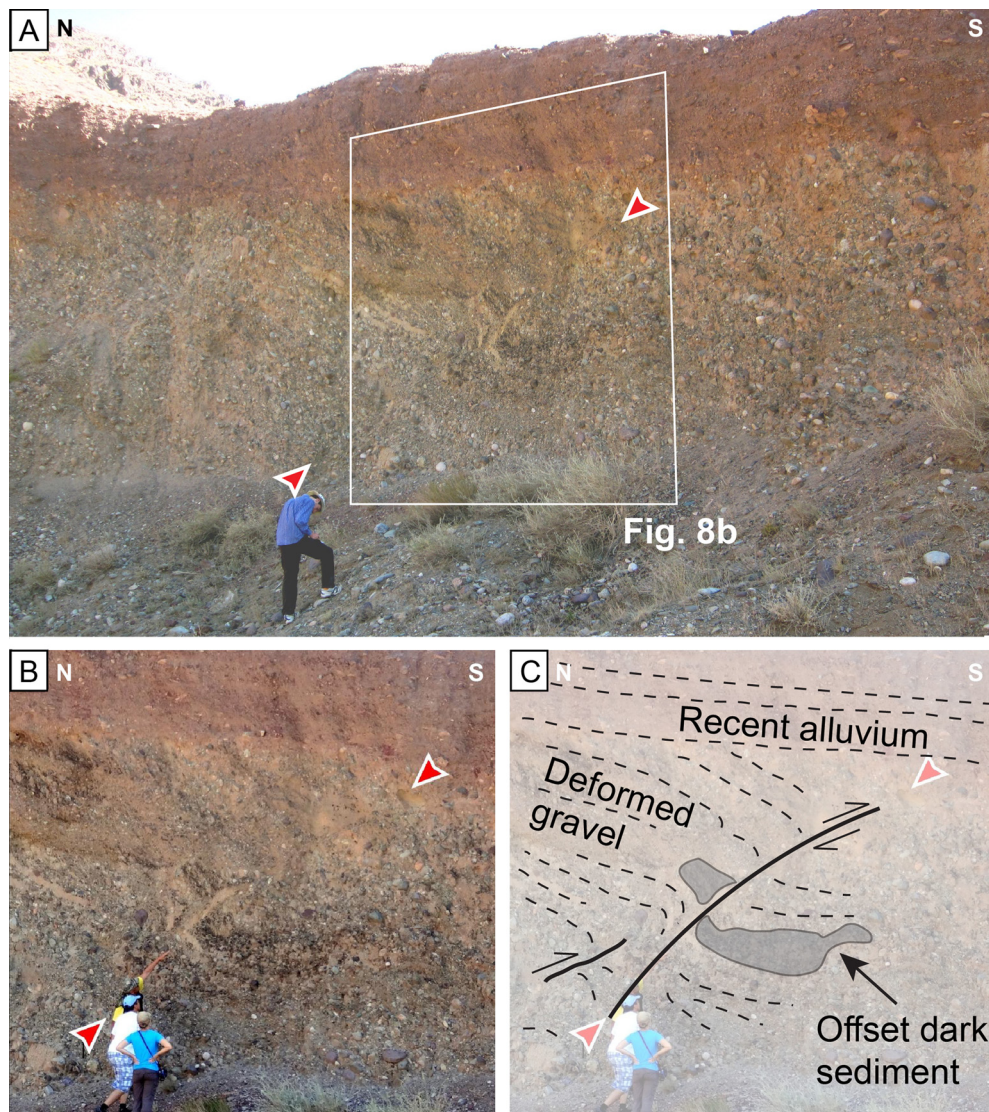
**Fig. 8.** On the northern site of the small basin, the Bartogai Fault offsetting gravel layers can be seen in a gravel pit (see Fig. 1 for location). The fault does not, however, produce a surface offset, which indicates that the scarp underwent erosion since the last surface rupturing earthquake. (A) View of the entire section, the fault is in the centre of the photo, marked by the red arrows. Note the undeformed reddish layer on top which is the most recent alluvial unit. (B) Close-up of the fault zone. (C) Geological interpretation of B. (For interpretation of the references to colour in this figure legend, the reader is referred to the web version of this article.)

samples from the palaeosol were used for radiocarbon dating (C1 and C2) since no charcoal, shell, or similar material was encountered. The age of the palaeosol should pre-date the last surface rupturing event. Bulk sample C1 from the palaeosol in the footwall gave a $2\sigma$ calibrated age of 7310–7175 BP; bulk sample C2 from the hanging wall has an age of 3640–3545 BP. This variation is most likely due to the fact that in bulk palaeosol samples material from a wide time span of soil formation processes is accumulated. Also, groundwater flow through the sediments can alter the apparent age. We interpret the older age of ∼7.2 ka BP as a maximum value, as older material from upslope areas of the alluvial fan might have been washed down and incorporated into the soil and the soil was probably stable for many thousands of years. The lower age of ∼3.6 ka BP probably marks the youngest stage of soil development. We therefore assume that the younger of the two values most immediately predates the earthquake.

All luminescence dating samples were collected using stainless steel tubes, hammered into clean vertical sections. The samples were subsequently processed at the University of Sheffield luminescence laboratory using a single grain post-IR IRSL K-feldspar dating approach. Under controlled laboratory lighting conditions,

sand-sized (180–212 µm) grains of K-feldspar were extracted from the inner part of each sample using a sodium polytungstate separation with a density of 2.565 g cm$^{-3}$, followed by a short 10% hydrofluoric (HF) acid treatment for 10 min to etch and clean the grain surfaces (Roder et al., 2012). This dating protocol was selected to overcome problems of low quartz sensitivity commonly encountered in regions characterized by active tectonics (Rhodes, 2011). Although feldspar post-IR IRSL is less rapidly reduced by light than quartz OSL (Roder et al., 2012; Smedley et al., 2015), the presence of many sensitive feldspar grains in bedrock samples, and in sediments derived from bedrock with little transport or weathering, provides the opportunity to measure this signal using single grains, and to isolate those grains that were well-bleached prior to deposition from those with residual IRSL signals owing to incomplete bleaching. The measurement protocol was modified for application to single grains from Buylaert et al. (2009), who isolated a thermally-stable component by measuring a second IRSL signal at 225 °C after the measurement of an IRSL signal at 50 °C. The protocol uses a preheat treatment of 60s at 250 °C before the measurement of the natural, regenerated or test-dose IRSL, and has been assessed in comparison to different samples from loca-

**Table 1**
Results from the radiocarbon dating of samples C1 and C2 and results from the IRSL dating of samples OSL 3–7. Radiocarbon dates are reported as radiocarbon years before present where present = AD 1950. By international convention the modern reference standard was 95% the $^{14}$C activity of the National Institute of Standards and Technology (NIST) Oxalic Acid (SRM 4990C) and calculated using the Libby $^{14}$C half life (5568). Conventional age represents the measured radiocarbon age corrected for isotopic fractionation. The calibrated result is calculated from the conventional age using the calibration curve INTCAL13 after Reimer et al. (2013). Single grain K-feldspar post-IR IRSL results are reported based on the minimum consistent single grain results, following the procedures described in the text, in the supplementary material, and by Rhodes (2015).

| Sample | $\delta^{13}$C (‰) | Conventional $^{14}$C age | $\pm 2\sigma$ | Calibrated $2\sigma$ age (BP) | Calibrated $1\sigma$ age (BP) |
|---|---|---|---|---|---|
| C1 | −17 | 6320 | 30 | 7310 to 7175 | 7270 to 7250 |
| C2 | −17.5 | 3340 | 30 | 3640 to 3545 | 3610 to 3560 |

| Sample | Lab code | Depth (m) | Equivalent dose (Gy) $\pm 1\sigma$ | Total dose rate (mGy/yr) $\pm 1\sigma$ | Age (ka before AD 2015) $\pm 1\sigma$ |
|---|---|---|---|---|---|
| KAZ14-BG-OSL3 | Shfd14075 | 1.10 | 74.6 ± 3.4 | 3.80 ± 0.16 | 17.7 ± 1.1 |
| KAZ14-BG-OSL4 | Shfd14076 | 1.30 | 182 ± 7 | 3.61 ± 0.16 | 44.0 ± 2.6 |
| KAZ14-BG-OSL5 | Shfd14077 | 1.30 | 175 ± 8 | 3.74 ± 0.16 | 39.9 ± 2.7 |
| KAZ14-BG-OSL6 | Shfd14078 | 0.35 | 14.0 ± 1.3 | 4.13 ± 0.19 | 3.15 ± 0.32 |
| KAZ14-BG-OSL7 | Shfd14079 | 0.80 | 27.7 ± 2.1 | 4.99 ± 0.25 | 5.87 ± 0.51 |

tions where the age was constrained by independent techniques (Rhodes, 2015). It has been applied to date several different contexts where the sediment age provides fault slip-rate or palaeoseismic constraint. The single grain post-IR IRSL dating protocol applied to the samples in this project was unchanged from that assessed by Rhodes (2015). The combined equivalent dose (De) values used in the age estimates presented in Table 1 were derived by excluding incompletely bleached grains (open symbols in Appendix J) until those remaining were mutually consistent with their measurement uncertainties plus an overdispersion value of 15% added in quadrature primarily to allow for the effects of variations in dose rate. Fading measurements confirmed very little anomalous fading was observed in these samples, and the ages presented are not corrected for this effect. Sediment dose rates were based on ICP-OES (K) and ICP-MS (U, Th) elemental determinations of the material taken from the end of each sample collection tube; an internal potassium concentration of 12.5 ± 1.0% was assumed to estimate the internal beta dose rate, based on Huntley and Baril (1997). Further technical details may be found in the supplementary material, along with plots showing the equivalent dose values measured for each sample. Sample OSL6 was taken from what we interpret as a colluvial wedge (unit 2; Fig. 6) and gave an age of 3.15 ± 0.32 ka. This age is younger than that of the two radiocarbon samples, which makes sense when the wedge formed immediately after the earthquake. Sample OSL7 comes from the palaeosol in the footwall of F1, close to sample C1, and returned an age of 5.87 ± 0.51 ka and lies within the age range bracketed by C1 and C2. These three samples from the palaeosol span ∼3.5 ka. One possible explanation for this mismatch is that bulk radiocarbon samples from soils contain organic material from different stages of soil formation and thus, a rather wide spread in ages can be expected. We interpret the radiocarbon samples to mirror a period of ongoing soil formation which lasted at least from ∼7.2 ka to 3.5 ka. The IRSL date returns the burial age of the non-organic sample material. We therefore interpret this age to reflect the incorporation of fine-grained sediment into the palaeosol, which may happen at any time during the soil formation, for example by wind or downslope wash during rain. Sample OSL3 from unit 4 should pre-date the last surface faulting, and post-date the penultimate fault (Figs. 6 and 8). This sample gave an age of 17.7 ± 1.1 ka, indicating that the penultimate surface rupture happened before the end of the LGM.

Sample OSL5 was taken from unit 6a, a silty layer in the footwall of fault F2, pre-dating the penultimate event. This sample has an age of 39.9 ± 2.7 ka. Finally, sample OSL4 from unit 6a in the

hanging-wall of F2 also predates the penultimate event and returned and age of 44.0 ± 2.6 ka. This is accordance with sample OSL5, as both samples pre-date the penultimate earthquake and the ages of the units overlap.

To conclude, radiocarbon and IRSL dating indicate that the last surface rupturing earthquake happened at fault F1 around 3.2 ka BP. The penultimate event at fault F2 occurred between 17.7 ± 1.1 and 39.9 ± 2.7 ka BP.

### 3.2.3. Morphological dating of the fault scarp

Scarp diffusion provides a method for morphological dating of scarps (e.g. Avouac, 1993; Hanks, 2000). This technique assumes that scarp degradation occurs as a diffusive process after scarp formation, and thus a geometrical analysis of the DGPS profiles allows estimating when the scarp was formed. Degradation over time $t$ (ka) is assumed to be proportional to the slope angle:

$$\frac{\partial u}{\partial t} = \kappa \frac{\delta^2 u}{\delta x^2} \tag{1}$$

where $u$ is the scarp height (m), $x$ is the distance along profile (m) and $\kappa$ is the mass diffusivity (m²/ka). Solving equation (1) for $\kappa t$ allows estimating the age of the scarp when the mass diffusivity for the study area is known. Diffusion ages $\kappa t$ are therefore given in m², as the real ages depend on the local $\kappa$-value. We used a MATLAB script which calculates the fault offset and slope angles as described in section 3.1. These values are used to calculate the diffusion age $\kappa t$, by analysing the near-field scarp profile and solving equation (1) for $\kappa t$ using the solution given by Andrews and Hanks (1985), as outlined in Walker et al. (2015). We estimate an uncertainty on the value of diffusion age by a Monte Carlo approach using the estimated uncertainty in the offset, fan slopes and also a range in our selection of initial scarp slope angle (35 ± 2°).

We analysed twelve DGPS profiles across the fault scarp at the trench site S1. Here, the scarp has a mean diffusivity age ($\kappa\tau$) of 21.9 ± 3.1 m² (Fig. 5B). No values for the mass diffusivity of this part of Kazakhstan are currently available. Avouac (1993) estimated a mass diffusivity of 5.5 ± 2 m²/ka for the Dzhungarian Basin, which has comparable lithology and climatic conditions. Applying this value returns a scarp age of ∼4 ± 1.6 ka. This age is consistent with the IRSL results, but yields a large error due to the uncertainty in the mass diffusivity. However, the close fit of the morphological dating and the results from independent age constraints indicates that a mass diffusivity of ∼5.5 ± 2 m²/ka can be assumed for our study area.

**Table 2**

Magnitude estimates based on different input values for the two most recent surface rupturing earthquakes (WC94: Wells and Coppersmith, 1994; HK79: Hanks and Kanamori, 1979). Note that the values derived from the vertical offsets measured with DGPS were calculated with a fault dip of 25° as seen in the trench.

| Fault | Magnitude relationship | Input value | Moment magnitude | Reference |
|---|---|---|---|---|
| Last event, F1 | Fault length (mapped) | 50 km | 7.1 | WC94 |
| | Fault length, visible scarp | 25 km | 6.7 | WC94 |
| | Area, 20 km depth, 45° dip, 25 km length | 700 km$^2$ | 6.9 | WC94 |
| | Area, 20 km depth, 45° dip, 50 km length | 1400 km$^2$ | 7.2 | WC94 |
| | Slip in trench | 3 m | 6.7–7.3 | WC94 |
| | Offset from DGPS, maximum displacement | 6.1 m | 6.9–7.3 | WC94 |
| | Seismic moment, 25 km length, 20 km width, 3 m slip | $6.4 \times 10^{19}$ N m | 7.2 | HK79 |
| | Seismic moment, 50 km length, 20 km width, 6.1 m slip | $26 \times 10^{19}$ N m | 7.6 | HK79 |
| F2 | Offset in trench, maximum | 0.63 m | 6.4–6.5 | WC94 |
| | Offset in trench, average | 0.63 m | 6.6–6.8 | WC94 |

*3.2.4. Palaeo-earthquake magnitudes*

For the most recent event we can estimate a moment magnitude based on empirical relationships between surface rupture length, fault length, rupture area, and amount of offset (Wells and Coppersmith, 1994). We emphasise that the reliability of the relationship between offset and magnitude for thrust faults suffers from low correlation. All estimates are shown in Table 2.

The rupture extends for a mapped length of ∼25 km, and yet the surface break may have extended along the entire 50 km fault length. We therefore use 25–50 km to give the minimum–maximum $M_w$ range of $M_w$ 6.7–7.1. We found 3 m of total slip in our trench excavation at a fault dip of 25°. The maximum scarp height from along the rupture was 2.6 m, which corresponds to 6.1 m of slip with a dip of 25°. The range of slip values yields $M_w$ 6.9–7.3. If the dip angle of the fault plane near the surface is variable along strike, a rather constant slip would also lead to a variation of the scarp height. Based on our observations we cannot distinguish between these cases or a combination of both.

For the fault area relationships we assume a seismogenic thickness of 20 km, which is typical for the earthquake depths in the region (Sloan et al., 2011; Krüger et al., 2015). We also use a fault dip of 45° instead of 25° as seen in the trench, as we suspect that the fault dip steepens at depth beneath the Toraigyr range. Relatively steep reverse faults with angles >45° are reported on faults within the NE Tien Shan region (e.g. Sloan et al., 2011; Selander et al., 2012; Kober et al., 2013; Campbell et al., 2015). Fault lengths of 25–50 km yield $M_w$ 6.9–7.2. Using the Hanks and Kanamori (1979) relationship to calculate moment from fault area and slip, with a rigidity of $\mu = 3 \times 10^{10}$ N m$^{-2}$, a slip of 3–6.1 m, a fault length of 25–50 km, and converting this value to $M_w$ results in magnitudes between $M_w$ 7.2 and $M_w$ 7.6.

Depending on whether we use the mapped rupture length of ∼25 km, or the overall fault length of 50 km, our measured slip of 3–6.1 m yields a slip to length ratio of between $0.6 \times 10^{-4}$ and $2.44 \times 10^{-4}$. These figures are within the range for global earthquakes (Scholz et al., 1986), but rather large. For the penultimate event we can only use the offset visible in the trench (∼0.6 m), which leads to an estimate of at least $M_w$ 6.5. As noted earlier, this offset should be considered a minimum, such that the magnitude of the penultimate event is likely to have been larger.

## 4. Discussion

Fault scarps generated by repeated surface rupturing are known throughout the Tien Shan (e.g. Tapponnier and Molnar, 1979; Avouac et al., 1993; Brown et al., 1998; Thompson et al., 2002; Korjenkov et al., 2006; Selander et al., 2012; Campbell et al., 2013, 2015) and they are commonly seen as clear evidence for active faulting. On the Toraigyr Fault we found evidence for two surface rupturing earthquakes in the last 39.9 ± 2.7 ka in a trench excavation. Only the most recent one (∼3.2 ka) has left visible evidence at the surface, apart from three remnants of larger scarps.

Since the penultimate event happened between 17.7 ± 1.1 and 39.9 ± 2.7 ka BP, we conclude that the landscape was reset since then, which resulted in the deposition and abandonment of the T1 fan surface.

The T1 fan surface could represent the 10–15 ka post-glacial terrace, which is widespread across the Kyrgyz Tien Shan (Thompson et al., 2002; Landgraf et al., 2016). Avouac et al. (1993) report a period of rapid fan accumulation at the beginning of the Holocene from the Chinese Tien Shan. They explain their observations with a general change to a warmer and wetter climate and with an increase of discharge due to melting of ice stored during the LGM. Poisson and Avouac (2004) also see a change of the erosional pattern and an increase of discharge at the onset of the Holocene, based on incision patterns in the Northern Tien Shan. In contrast, Brown et al. (1998) studied alluvial fans in the southern Tien Shan and found that they were abandoned during the LGM and not after 22 ka. Molnar et al. (1994) show that abandonment and incision of flood plains does not solely occur after the last glacier retreat. Glaciation patterns indicate that the local LGM in the Tien Shan generally preceded the global LGM but did not result in large-scale ice advances (Lifton et al., 2014 and the references therein). Instead, local variations in climate seem to have occurred. T1 might therefore be older than 10–15 ka. Both cases – a change in erosion pattern during or after the LGM – fit our data because we can only bracket the penultimate earthquake between 17.7 ± 1.1 and 39.9 ± 2.7 ka BP.

Along the Toraigyr Fault, the landscape reset has obliterated the morphological expression of surface faulting that occurred before the LGM. As a consequence, faults with recurrence intervals exceeding 10–15 ka may appear as inactive if they have not ruptured since the end of the LGM. Recent studies show that in the Tien Shan the recurrence intervals of great earthquakes can indeed be exceptionally long on some, if not many, faults (e.g. Prentice et al., 2002; Campbell et al., 2015; Abdrakhmatov et al., 2016). Our interpretation is supported by similar observations from the neighbouring faults. The ENE-WSW striking Chon Kemin–Chilik Fault zone, the local segment of which is named Bartogai Fault by Ostropiko et al. (1987), is a major strike-slip feature with a vertical component of motion (Delvaux et al., 2001; Selander et al., 2012). It bounds the Toraigyr Fault to the west and forms the northern margin of the basin (Fig. 1B). Close to the Bartogai reservoir the fault offsets and deforms alluvial fan material in a gravel pit, but is capped by undistorted sediments and does not have a surface expression (Fig. 8). To the SE of the Toraigyr Fault the south margin of the Ili Basin exhibits a prominent range front, but no fault scarps clearly offset the alluvial fans there (Fig. 1B). This might be another case where any traces of Late Quaternary faulting were obliterated by erosion and sedimentation due to long earthquake repeat times.

Recent studies and our data show that in the Tien Shan, the lack of fault scarps is not a sufficient condition for identifying a

fault as inactive. Relatively young ruptures may also be buried under alluvial fan material. Many faults here have very extraordinarily long recurrence intervals, as in general strain rates are moderate and the faults tend to break in great, but rare earthquakes (Campbell et al., 2013, 2015). This problem might also be present in other parts of Central Asia, for example in the low-strain areas of Mongolia (e.g. Rizza et al., 2015; Walker et al., 2015). It may also be applicable in other continental interior settings.

## 5. Conclusions

We show that faults in the Tien Shan may have very long recurrence intervals for surface rupturing events. Consequently, the surface expressions of these faults can be obliterated by erosional/depositional events, which mask evidence of Pleistocene activity. The absence of fault scarps and similar morphological indicators can thus not be regarded as evidence for fault inactivity. Our study shows the value of palaeoseismological investigations when instrumental and historical seismicity records are short with respect to earthquake recurrence intervals. It also highlights challenges, as active faults with little or no surface expression will be overlooked and the seismic hazard posed by them will be underestimated. The lack of morphological evidence for active faulting on faults that ruptured in the Late Quaternary may also hinder our understanding of how a part of the convergent motion between India in Eurasia is accommodated in the Tien Shan.

## Acknowledgements

## Appendix. Supplementary data

Supplementary data associated with this article can be found in the online version at http://dx.doi.org/10.1016/j.epsl.2016.11.025. These data include the Google map of the most important areas described in this article.

## References

Abdrakhmatov, K.Y., Aldazhanov, S.A., Hager, B.H., Hamburger, M.W., Herring, T.A., Kalabaev, K.B., Makarov, V.I., Molnar, P., Panasyuk, S.V., Prilepin, M.T., Reilinger, R.E., Sadybakasovstar, I.S., Souter, B.J., Trapeznikov, Yu.A., Tsurkov, V.Ye., Zubovich, A.V., 1996. Relatively recent construction of the Tien Shan inferred from GPS measurements of present-day crustal deformation rates. Nature 384, 450–453. http://dx.doi.org/10.1038/384450a0.

Abdrakhmatov, K., Walker, R.T., Campbell, G.E., Carr, A.S., Elliott, A., Hillemann, C., Hollingsworth, J., Landgraf, A., Mackenzie, D., Mukambayev, A., Rizza, M., Sloan, R.A., 2016. Multi-segment rupture in the July 11th 1889 Chilik earthquake (Mw 8.0–8.3), Kazakh Tien Shan, identified from remote-sensing, field survey, and palaeoseismic trenching. J. Geophys. Res., Solid Earth 121 (6), 4615–4640. http://dx.doi.org/10.1002/2015JB012763.

Andrews, D.J., Hanks, T.C., 1985. Scarp degraded by linear diffusion: inverse solution for age. J. Geophys. Res., Solid Earth 90 (B12), 10193–10208. http://dx.doi.org/10.1029/JB090iB12p10193.

Arrowsmith, R., Crosby, C., Korjenkov, A., Mamyrov, E., Povolotskaya, I., Guralnik, B., Landgraf, A., 2016. Surface rupture of the 1911 Kebin (Chon-Kemin) earthquake, Northern Tien Shan, Kyrgyzstan. Geol. Soc. (Lond.) Spec. Publ. 432. http://dx.doi.org/10.1144/SP432.10.

Avouac, J., 1993. Analysis of scarp profiles: evaluation of errors in morphologic dating. J. Geol. Res. 98, 6745–6754. http://dx.doi.org/10.1029/92JB01962.

Avouac, J.P., Tapponnier, P., 1993. Kinematic model of active deformation in central Asia. Geophys. Res. Lett. 20 (10), 895–898. http://dx.doi.org/10.1029/93GL00128.

Avouac, J.P., Tapponnier, P., Bai, M., You, H., Wang, G., 1993. Active thrusting and folding along the northern Tien Shan and late Cenozoic rotation of the Tarim relative to Dzungaria and Kazakhstan. J. Geophys. Res., Solid Earth 98 (B4), 6755–6804. http://dx.doi.org/10.1029/92JB01963.

Bindi, D., Parolai, S., Gómez-Capera, A., Locati, M., Kalmetyeva, Z., Mikhailova, N., 2014. Locations and magnitudes of earthquakes in Central Asia from seismic intensity data. J. Seismol. 18 (1), 1–21. http://dx.doi.org/10.1007/s10950-013-9392-1.

Bogdanovich, K.I., Kark, I.M., Korolkov, B.Y., Mushketov, D.I., 1914. Earthquake in Northern District of Tien Shan, 22 December 1910 (4 January 1911). Commission of the Geology Committee, Leningrad (in Russian).

Brown, E.T., Bourlés, D.L., Burchfiel, B.C., Qidong, D., Jun, L., Molnar, P., Raisbeck, G.M., Yiou, F., 1998. Estimation of slip rates in the southern Tien Shan using cosmic ray exposure dates of abandoned alluvial fans. Geol. Soc. Am. Bull. 110 (3), 377–386. http://dx.doi.org/10.1130/0016-7606(1998)110<0377:EOSRIT>2.3.CO;2.

Burtman, V.S., 1975. Structural geology of variscan Tien Shan, USSR. Am. J. Sci. 275, 157–186.

Buylaert, J.P., Murray, A.S., Thomsen, K.J., Jain, M., 2009. Testing the potential of an elevated temperature IRSL signal from K-feldspar. Radiat. Meas. 44, 560–565.

Campbell, G.E., Walker, R.T., Abdrakhmatov, K., Schwenninger, J.L., Jackson, J., Elliott, J.R., Copley, A., 2013. The Dzhungarian fault: late quaternary tectonics and slip rate of a major right-lateral strike-slip fault in the northern Tien Shan region. J. Geophys. Res., Solid Earth 118 (10), 5681–5698. http://dx.doi.org/10.1002/jgrb.50367.

Campbell, G.E., Walker, R.T., Abdrakhmatov, K., Jackson, J., Elliott, J.R., Mackenzie, D., Middleton, T., Schwenninger, J.L., 2015. Great earthquakes in low strain rate continental interiors: an example from SE Kazakhstan. J. Geophys. Res., Solid Earth 120 (8), 5507–5534. http://dx.doi.org/10.1002/2015JB011925.

CMT, 2016. Global Centroid–Moment–Tensor (CMT) catalog. CMT catalog web search, http://www.globalcmt.org/CMTsearch.html. Last access 25 January 2016.

Cording, A., Hetzel, R., Kober, M., Kley, J., 2014. $^{10}$Be exposure dating of river terraces at the southern mountain front of the Dzungarian Alatau (SE Kazakhstan) reveals rate of thrust faulting over the past ∼400 ka. Quat. Res. 81 (1), 168–178. http://dx.doi.org/10.1016/j.yqres.2013.10.016.

Crosby, C., Arrowsmith, J., Korjenkov, A., Guralnik, B., Mamyrov, E., Povolotskaya, I., 2007. The hunt for surface rupture from the 1889 Ms 8.3 Chilik earthquake, Northern Tien-Shan, Kyrgyzstan and Kazakhstan. In: AGU Fall Meeting Abstracts, F5, poster presentation.

Delvaux, D., Abdrakhmatov, K.E., Lemzin, I.N., Strom, A.L., 2001. Landslide and surface breaks of the 1911 M 8.2 Kemin Earthquake. Russ. Geol. Geophys. 42 (10), 1583–1592.

Engdahl, E., Van Der Hilst, R., Buland, R., 1998. Global teleseismic earthquake relocation with improved travel times and procedures for depth determination. Bull. Seismol. Soc. Am. 88 (3), 722–743.

Hanks, T.C., 2000. The age of scarplike landforms from diffusion-equation analysis. In: Noller, J.S., Sowers, J.M., Lettis, W.R. (Eds.), Quaternary Geochronology: Methods and Applications. American Geophysical Union, Washington, DC.

Hanks, T.C., Kanamori, H., 1979. A moment magnitude scale. J. Geophys. Res. B 84 (B5), 2348–2350. http://dx.doi.org/10.1029/JB084iB05p02348.

Hendrix, M.S., Graham, S.A., Carroll, A.R., Sobel, E.R., McKnight, C.L., Schulein, B.J., Wang, Z., 1992. Sedimentary record and climatic implications of recurrent deformation in the Tian Shan: evidence from Mesozoic strata of the north Tarim, south Junggar, and Turpan basins, northwest China. Geol. Soc. Am. Bull. 104 (1), 53–79. http://dx.doi.org/10.1130/0016-7606(1992)104<0053:SRACIO>2.3.CO;2.

Huntley, D.J., Baril, M.R., 1997. The K-content of the K-feldspars being measured in optical dating or in thermoluminescence dating. Ancient TL 15, 11–13.

ISC, 2016. International Seismological Centre, on-line catalogue. http://www.isc.ac.uk. International Seismological Centre, Thatcham, UK. Last access 7 March 2016.

Johnson, K., Nissen, E., Saripalli, S., Arrowsmith, J.R., McGarey, P., Scharer, K., Williams, P., Blisniuk, K., 2014. Rapid mapping of ultrafine fault zone topography with structure from motion. Geosphere 10 (5), 969–986. http://dx.doi.org/10.1130/GES01017.1.

Kober, M., Seib, N., Kley, J., Voigt, T., 2013. Thick-skinned thrusting in the northern Tien Shan foreland, Kazakhstan: structural inheritance and polyphase deformation. Geol. Soc. (Lond.) Spec. Publ. 377 (1), 19–42. http://dx.doi.org/10.1144/SP377.7.

Korjenkov, A.M., Arrowsmith, J.R., Crosby, C., Mamyrov, E., Orlova, L.A., Povolotskaya, I.E., Tabaldiev, K., 2006. Seismogenic destruction of the Kamenka medieval fortress, northern Issyk-Kul region, Tien Shan (Kyrgyzstan). J. Seismol. 10 (4), 431–442. http://dx.doi.org/10.1007/s10950-006-9029-8.

Krüger, F., Kulikova, G., Landgraf, A., 2015. Instrumental magnitude constraints for the 11 July 1889, Chilik earthquake. Geol. Soc. (Lond.) Spec. Publ. 432, SP432–SP438. http://dx.doi.org/10.1144/SP432.8.

Kulikova, G., Krüger, F., 2015. Source process of the 1911 M8.0 Chon–Kemin earthquake: investigation results by analogue seismic records. Geophys. J. Int. 201, 1891–1911. http://dx.doi.org/10.1093/gji/ggv091.

Landgraf, A., Dzhumabaeva, A., Abdrakhmatov, K., Macaulay, E.A., Strecker, M.R., Arrowsmith, J.R., Preusser, F., Rugel, G., Merchel, S., 2016. Repeated large-magnitude earthquakes in a tectonically active, low-strain continental interior: the northern Tien Shan, Kyrgyzstan. J. Geophys. Res., Solid Earth 121 (5), 3888–3910. http://dx.doi.org/10.1002/2015JB012714.

Lifton, N., Beel, C., Hättestrand, C., Kassab, C., Rogozhina, I., Heermance, R., Oskin, M., Burbank, D., Blomdin, R., Gribenski, N., Caffee, M., Goehring, B.M., Heyman, J., Ivanov, M., Li, Y., Li, Y., Petrakov, D., Usubaliev, R., Codilean, A.T., Chen, Y., Harbor, Stroeven, A.P., 2014. Constraints on the late Quaternary glacial history of the Inylchek and Sary-Dzaz valleys from in situ cosmogenic $^{10}$Be and $^{26}$Al, eastern Kyrgyz Tian Shan. Quat. Sci. Rev. 101, 77–90.

Molnar, P., Tapponnier, P., 1975. Cenozoic tectonics of Asia: effects of a continental collision. Science 189 (4201), 419–426. http://dx.doi.org/10.1126/science.189.4201.419.

Molnar, P., Brown, E.T., Burchfiel, B.C., Deng, Q., Feng, X., Li, J., Raisbeck, G.B., Shi, J., Zhangming, W., Yiou, F., You, H., 1994. Quaternary climate change and the formation of river terraces across growing anticlines on the north flank of the Tien Shan, China. J. Geol. 102 (5), 583–602. http://dx.doi.org/10.1086/629700.

Ostropiko, P.A., Kartashov, A.P., Atrushkevich, P.A., 1987. Construction of geodetic networks for studying crustal movements when creating hydraulic structures in seismic regions. Hydrotech. Constr. 21 (3), 145–150. http://dx.doi.org/10.1007/BF01424002.

Poisson, B., Avouac, J.P., 2004. Holocene hydrological changes inferred from alluvial stream entrenchment in north Tian Shan (northwestern China). J. Geol. 112 (2), 231–249. http://dx.doi.org/10.1086/381659.

Prentice, C.S., Kendrick, K., Berryman, K., Bayasgalan, A., Ritz, J.F., Spencer, J.Q., 2002. Prehistoric ruptures of the Gurvan Bulag fault, Gobi Altay, Mongolia. J. Geophys. Res., Solid Earth 107 (B12). http://dx.doi.org/10.1029/2001JB000803.

Reimer, P.J., Bard, E., Bayliss, A., Beck, J.W., Blackwell, P.G., Bronk Ramsey, C., Buck, C.E., Cheng, H., Edwards, R.L., Friedrich, M., Grootes, P.M., Guilderson, T.P., Haflidason, H., Hajdas, I., Hatté, C., Heaton, T.J., Hoffmann, D.L., Hogg, A.G., Hughen, K.A., Kaiser, K.F., Kromer, B., Manning, S.W., Niu, M., Reimer, R.W., Richards, D.A., Scott, E.M., Southon, J.R., Staff, R.A., Turney, C.S.M., van der Plicht, J., 2013. IntCal13 and Marine13 radiocarbon age calibration curves 0–50,000 years cal BP. Radiocarbon 55 (4), 1869–1887. http://dx.doi.org/10.1017/S0033822200048864.

Rhodes, E.J., 2011. Optically stimulated luminescence dating of sediments over the past 200,000 years. Annu. Rev. Earth Planet. Sci. 39, 461–488. http://dx.doi.org/10.1146/annurev-earth-040610-133425.

Rhodes, E.J., 2015. Dating sediments using potassium feldspar single-grain IRSL: initial methodological considerations. Quat. Int. 362, 14–22. http://dx.doi.org/10.1016/j.quaint.2014.12.012.

Rizza, M., Ritz, J.F., Prentice, C., Vassallo, R., Braucher, R., Larroque, C., Arzhannikova, A., Arzhannikov, S., Mahan, S., Massault, M., Michelot, J.L., Todbileg, M., ASTER Team, 2015. Earthquake geology of the Bulnay Fault (Mongolia). Bull. Seismol. Soc. Am. 105 (1), 72–93. http://dx.doi.org/10.1785/0120140119.

Roder, B.J., Lawson, M.J., Rhodes, E.J., Dolan, J.F., McAuliffe, L., McGill, S.F., 2012. Assessing the potential of luminescence dating for fault slip rate studies on the Garlock fault, Mojave Desert, California, USA. Quat. Geochronol. 10, 285–290. http://dx.doi.org/10.1016/j.quageo.2012.03.013.

Scholz, C.H., Aviles, C.A., Wesnousky, S.G., 1986. Scaling differences between large interplate and intraplate earthquakes. Bull. Seismol. Soc. Am. 76 (1), 65–70.

Selander, J., Oskin, M., Ormukov, C., Abdrakhmatov, K., 2012. Inherited strike-slip faults as an origin for basement-cored uplifts: example of the Kungey and Zailiskey ranges, northern Tian Shan. Tectonics 31 (4). http://dx.doi.org/10.1029/2011TC003002.

Sloan, R.A., Jackson, J.A., McKenzie, D., Priestley, K., 2011. Earthquake depth distributions in central Asia, and their relations with lithosphere thickness, shortening and extension. Geophys. J. Int. 185 (1), 1–29. http://dx.doi.org/10.1111/j.1365-246X.2010.04882.x.

Smedley, R.K., Duller, G.A.T., Roberts, H.M., 2015. Bleaching of the post-IR IRSL signal from individual grains of K-feldspar: implications for single-grain dating. Radiat. Meas. 79, 33–42. http://dx.doi.org/10.1016/j.radmeas.2015.06.003.

Tapponnier, P., Molnar, P., 1979. Active faulting and Cenozoic tectonics of the Tien Shan, Mongolia, and Baikal regions. J. Geophys. Res., Solid Earth 84 (B7), 3425–3459. http://dx.doi.org/10.1029/JB084iB07p03425.

Thompson, S.C., Weldon, R.J., Rubin, C.M., Abdrakhmatov, K., Molnar, P., Berger, G.W., 2002. Late Quaternary slip rates across the central Tien Shan, Kyrgyzstan, central Asia. J. Geophys. Res., Solid Earth 107 (B9), ETG-7. http://dx.doi.org/10.1029/2001JB000596.

Walker, R.T., Wegmann, K., Bayasgalan, A., Carson, R., Elliott, J.R., Fox, M., Nissen, E.K., Sloan, R.A., 2015. The Egiin Davaa prehistoric rupture, central Mongolia: a large-magnitude normal faulting earthquake, on a reactivated fault with little cumulative slip, in a slowly deforming continental interior. Geol. Soc. (Lond.) Spec. Publ. 432. http://dx.doi.org/10.1144/SP432.4.

Wallace, R.E., 1977. Profiles and ages of young fault scarps, north-central Nevada. Geol. Soc. Am. Bull. 88 (9), 1267–1281. http://dx.doi.org/10.1130/0016-7606(1977)88<1267:PAAOYF>2.0.CO;2.

Wells, D.L., Coppersmith, K.J., 1994. New empirical relationships among magnitude, rupture length, rupture width, rupture area, and surface displacement. Bull. Seismol. Soc. Am. 84 (4), 974–1002.

Wessel, P., Smith, W.H., 1998. New improved version of generic mapping tools released. Eos Trans. AGU 79 (47), 579. http://dx.doi.org/10.1029/98EO00426.

Zubovich, A.V., Wang, X., Scherba, Y.G., Schelochkov, G.G., Reilinger, R., Reigber, C., Mosienko, O.I., Molnar, P., Michajljow, W., Makarov, V.I., Li, J., Kuzikov, S.I., Herring, T.A., Hamburger, M.W., Hager, B.H., Dang, Y., Bragin, V.D., Beisenbaev, R.T., 2010. GPS velocity field for the Tien Shan and surrounding regions. Tectonics 29. http://dx.doi.org/10.1029/2010TC002772.